

Difference Image Analysis: Extension to a Spatially Varying Photometric Scale Factor and Other Considerations

D. M. Bramich^{1*}, Keith Horne², M. D. Albrow³, Y. Tsapras^{4,5}, C. Snodgrass⁶,
R. A. Street⁴, M. Hundertmark², Noé Kains¹, A. Arellano Ferro⁷, R. Figuera Jaimes⁷
and Sunetra Giridhar⁸

¹European Southern Observatory, Karl-Schwarzschild-Straße 2, 85748 Garching bei München, Germany

²SUPA Physics & Astronomy, North Haugh, St Andrews, KY16 9SS, Scotland, UK

³Department of Physics and Astronomy, Private Bag 4800, University of Canterbury, New Zealand

⁴Las Cumbres Observatory, 6740B Cortona Dr, Suite 102, Goleta, CA 93117, USA

⁵School of Physics and Astronomy, Queen Mary University of London, Mile End Road, London E1 4NS, England

⁶Max Planck Institute for Solar System Research, Max-Planck-Str. 2, 37191 Katlenburg-Lindau, Germany

⁷Instituto de Astronomía, Universidad Nacional Autónoma de México, México

⁸Indian Institute of Astrophysics, Koramangala 560034, Bangalore, India

Accepted 2010 August ???. Received 2010 August ???. Submitted 2010 August ???

ABSTRACT

We present a general framework for matching the point-spread function (PSF), photometric scaling, and sky background between two images, a subject which is commonly referred to as difference image analysis (DIA). We introduce the new concept of a spatially varying photometric scale factor which will be important for DIA applied to wide-field imaging data in order to adapt to transparency and airmass variations across the field-of-view. Furthermore, we demonstrate how to separately control the degree of spatial variation of each kernel basis function, the photometric scale factor, and the differential sky background. We discuss the common choices for kernel basis functions within our framework, and we introduce the mixed-resolution delta basis functions to address the problem of the size of the least-squares problem to be solved when using delta basis functions. We validate and demonstrate our algorithm on simulated and real data. We also describe a number of useful optimisations that may be capitalised on during the construction of the least-squares matrix and which have not been reported previously. We pay special attention to presenting a clear notation for the DIA equations which are set out in a way that will hopefully encourage developers to tackle the implementation of DIA software.

Key words: methods: statistical - techniques: image processing - techniques: photometric

1 INTRODUCTION

Difference image analysis (DIA) aims to measure changes, from one image to another, in the objects that make up a scene. In astronomy, the objects are typically point sources changing in brightness or moving on the sky. Astronomical images are formed on a discrete detector array, after the sky scene suffers attenuation, geometrical distortion and blurring by the atmosphere and optics, superimposed on a sky background, and corrupted by detector noise. All of these effects are to different degrees non-uniform across the scene and variable on a variety of timescales. Furthermore, pairs of images of the same scene may suffer small misalignments in position or scale, or gross rotational misalignments.

The changes in object properties that we wish to measure are thus entangled with changes in the sky-to-detector, or scene-to-image, transformation. A residual difference image, formed by simple subtraction of one image from another, is generally dominated by changes in the transformation. To extract the astronomical information, we must accurately model the changes in astrometry, throughput, background, and blurring between the two images. We may then make corrections to match these effects from one image to another and subtract to form “cleaner” difference images, or we may model the original images including changes in both object properties and image transformations. While current DIA techniques are based on the former approach, we advocate the latter.

The model adopted to represent changes in the scene-to-image transformation must include the following differential (or corrective) components:

* E-mail: dbramich@eso.org, dan.bramich@hotmail.co.uk

- A coordinate transformation between the coordinate systems of each image to correct for image misalignments and/or differences in distortion.
- A photometric scaling that corrects for the changes in the attenuating effects of the atmosphere (and possibly the telescope optics) and differences in exposure time.
- A background offset that corrects for changes in the sky background emission.
- A convolution transformation that corrects for the changes in the image point-spread function (PSF) as a result of changes in atmospheric conditions and/or the telescope optics (e.g. focus changes).

Note that all of these components model differential corrections, not absolute values (e.g. the convolution transformation models the *change* in PSF shape between images, not the PSF itself).

The state of the art in DIA includes the components for photometric scaling, sky background offsets, and PSF convolution in the DIA modelling process. Recent developments (Bramich 2008, from now on B08) also include fractional pixel translations in the model. Other image misalignments (rotation, scale, shear, distortion) are corrected by pre-registering the images before application of DIA, usually involving image resampling.

The framework for the current approach to DIA was introduced by Alard & Lupton (1998) (from now on A98) for matching a reference image to a target image. The convolution kernel (including the photometric scaling) to be applied to the reference image is decomposed into a set of basis functions, and the differential background offset is included as a polynomial of the image coordinates, which converts the problem of finding the corrective components to a standard linear least-squares formulation. A follow-up paper by Alard (2000) (from now on A00) showed how the spatial variation of the convolution kernel can be modelled by multiplying the kernel basis functions by polynomials of the image coordinates. The kernel basis functions chosen by A98 and A00 are Gaussians of different widths, modified by polynomials of the kernel coordinates. The user must specify the number of Gaussian basis functions to be employed, their associated widths, and the degrees of the modifying polynomials. However, the optimal choice of parameters for generating the kernel basis functions is not obvious, although some investigation into this matter has been performed (Israel, Hessman & Schuh 2007).

It is clearly desirable to find a set of kernel basis functions that are inherently simple, thereby being specified by a minimal parameter set, and yet that can model the kernel with sufficient flexibility. A step towards this paradigm was made by B08 with the proposed representation of the kernel as a discrete pixel array where the kernel pixel values are solved for directly. This approach limits the requirements on the user to specifying the kernel size (and shape), and the kernel model is maximally flexible in modelling the most complicated convolution kernels (e.g. telescope jumps). B08 show that the new formulation is capable of modelling fractional pixel translations as part of the convolution kernel, thereby relaxing the requirement on image registration such that images need only be aligned to the nearest pixel before application of DIA. Spatial variation of the kernel is handled by interpolation of kernel and differential background solutions on a grid.

Soon after B08, Miller, Pennypacker & White (2008) (from now on M08) specified a set of kernel basis functions built from delta-functions centred at different kernel coordinates. This choice of basis functions leads to a solution that happens to be equivalent to the B08 solution (see Section 3.2), but it is specified such that it

fits into the A98 framework of equations. M08 also included a polynomial spatial variation of the delta-function coefficients to model the kernel spatial variation. Quinn, Clocchiatti & Hamuy (2010) “rediscovered” the M08 work, but failed to impose any control on the photometric scaling while also fixing the value of the central kernel pixel, leading to a sub-optimal kernel model that cannot freely model fractional pixel translations.

The choice of kernel basis functions in the A98 framework is fully down to the developer/user. While the delta-function basis (or delta basis for short) is very compelling, the number of free parameters grows quickly with the adopted kernel size. Hence it makes sense to choose some coarser functions in the outer part of the kernel where there is little variation or signal/amplitude. Albrow et al. (2009) introduce the idea of binned kernel pixels in the outer part of the kernel, which greatly reduces the number of kernel parameters, and Yuan & Akerlof (2008) introduce a bicubic *B*-splines basis.

One of the assumptions in the A98 DIA framework is that the photometric scaling between the reference image and the target image is characterised by a single number, which may be a reasonable assumption for images covering a small field-of-view (FOV), where spatial variations in atmospheric transparency and airmass are generally negligible. However, DIA is now being applied in projects that generate images covering multiple square degrees each (e.g. Palomar Transient Factory - Rau et al. 2009 and Law et al. 2009, PanSTARRS - Kaiser et al. 2010), where non-uniform transparency is common (due to passing clouds) and extinction varies from one edge of the image to another due to airmass gradients across the field. Extension of the DIA framework to a spatially varying photometric scale factor is therefore a necessary generalisation in the application of DIA to these projects.

In Section 2, we take the step of generalising DIA to be able to cope with a spatially varying photometric scale factor, while simultaneously modelling the spatial variation of the kernel shape and differential background. In presenting this generalised formulation, we also take the opportunity to present a clear set of DIA equations, with user-friendly notation, grouped in a logical way. The original DIA formulations in the literature (A98; A00) are not so transparent in this respect, and the M08 formulation where delta basis functions are introduced omits the consideration of pixel uncertainties, has difficult notation, and misses a number of important simplifications with respect to this kernel basis (see Section 3.2). Discussion of the most popular choices for the kernel basis functions and their implications with regard to the DIA formulation is made in Section 3, where we also introduce the mixed-resolution delta basis functions. In Section 4, we validate our algorithm using simulated data and we demonstrate it using some real data. Section 5 has been written to provide some implementation and optimisation hints for the DIA developer, and the methodology that we propose will help to make the DIA algorithms more feasible with respect to the increasing data volume (image sizes and numbers) from the latest generation of time-series imaging projects. Finally, we state our conclusions in Section 6.

2 THE GENERAL DIFFERENCE IMAGE ANALYSIS FORMULATION AND SOLUTION

In this Section, we derive a general theoretical formulation of the difference image analysis problem from which all previously published formulations arise as special cases. This generalisation allows us to exercise control separately over the spatial variation of

each kernel basis function, the photometric scale factor, and the differential sky background, as we show in Sections 2.1 & 2.3.

2.1 Defining The Target Image Model

We start as in B08 by considering a pair of registered images sampled on the same pixel grid, one being the reference image with pixel values R_{ij} , and the other the target image with pixel values I_{ij} , where i and j are pixel indices referring to the column i and row j of the image. We denote the spatial coordinate system in these images by (x, y) , and the (i, j) th pixel by (x_i, y_j) . Exact image registration is not strictly necessary, since the best formulations for the kernel model include corrections for translational (but not rotational or otherwise) image misalignments, which has the advantage of avoiding problematic image interpolation in many cases.

As first formulated by A98, we construct the model $M(x, y)$ for the target image as the reference image convolved with a spatially varying kernel $K(u, v, x, y)$ (where u and v are kernel coordinates) plus a spatially varying differential background $B(x, y)$:

$$M(x, y) = [R \otimes K](x, y) + B(x, y) \quad (1)$$

We wish to determine the best-fit convolution kernel and differential background, and to do this we must first make further assumptions about their functional form. We note that since the reference image is part of the target image model, it may be desirable to also determine the reference image pixel values R_{ij} . However, finding a solution to this issue is outside the scope of this paper.

A98 made the important step of decomposing the kernel into a set of basis functions thereby linearising the expression in Equation 1. Subsequently, A00 generalised the kernel decomposition to include the spatial variation of the basis function coefficients, which facilitated the modelling of the spatial variation of the kernel. We form the same kernel decomposition:

$$K(u, v, x, y) = \sum_{q=1}^{N_K} a_q(x, y) \kappa_q(u, v) \quad (2)$$

where $\kappa_q(u, v)$ is the q th kernel basis function, $a_q(x, y)$ is the q th spatially variable coefficient, and N_K is the number of kernel basis functions.

A polynomial is a sensible choice of model for the spatial variation of the kernel basis function coefficients since it respects the linearity of the decomposition in Equation 2, and by specifying the polynomial degree, one may control the amount of spatial variation that is to be modelled. The polynomial form for $a_q(x, y)$ was adopted by A00 with the same degree for each basis function coefficient. We generalise this further by modelling each coefficient as a polynomial with individual degree d_q , providing a flexibility that we require later on:

$$a_q(x, y) = \sum_{m=0}^{d_q} \sum_{n=0}^{d_q-m} a_{qmn} \eta(x)^m \xi(y)^n \quad (3)$$

where the a_{qmn} are polynomial coefficients for the q th kernel basis function. The coordinates $(\eta(x), \xi(y))$ are normalised spatial coordinates defined by:

$$\eta(x) = (x - x_c)/N_x \quad (4)$$

$$\xi(y) = (y - y_c)/N_y \quad (5)$$

which follow from the Taylor expansion of the spatial coordinates (x, y) around the image centre (x_c, y_c) for an image of size $N_x \times N_y$

pixels. This coordinate conversion improves the orthogonality of the spatial polynomial terms¹, and it prevents the significant polynomial coefficients from becoming progressively smaller for the higher order polynomial terms.

As in A98, we also adopt a polynomial model of degree d_B for the differential background:

$$B(x, y) = \sum_{k=0}^{d_B} \sum_{l=0}^{d_B-k} b_{kl} \eta(x)^k \xi(y)^l \quad (6)$$

where the b_{kl} are the polynomial coefficients.

We now have a model $M(x, y)$ for the target image that is a linear combination of functions of x and y . This is easily shown by substituting Equations 2, 3 & 6 into Equation 1 and using the fact that convolution is distributive:

$$M(x, y) = \sum_{q=1}^{N_K} [R \otimes \kappa_q](x, y) \sum_{m=0}^{d_q} \sum_{n=0}^{d_q-m} a_{qmn} \eta(x)^m \xi(y)^n + \sum_{k=0}^{d_B} \sum_{l=0}^{d_B-k} b_{kl} \eta(x)^k \xi(y)^l \quad (7)$$

The target image is a discrete image of pixel values I_{ij} and therefore we wish to evaluate the model for the target image at the discrete pixel coordinates (x_i, y_j) . Let us use M_{ij} to represent the discrete model image $M(x_i, y_j)$ and (η_i, ξ_j) to represent the discrete coordinate array $(\eta(x_i), \xi(y_j))$. Then, using the fact that the convolution of the reference image R_{ij} with the continuous kernel basis function $\kappa_q(u, v)$ is equivalent to a discrete convolution (see Appendix A), we have:

$$M_{ij} = \sum_{q=1}^{N_K} [R \otimes \kappa_q]_{ij} \sum_{m=0}^{d_q} \sum_{n=0}^{d_q-m} a_{qmn} \eta_i^m \xi_j^n + \sum_{k=0}^{d_B} \sum_{l=0}^{d_B-k} b_{kl} \eta_i^k \xi_j^l \quad (8)$$

with:

$$[R \otimes \kappa_q]_{ij} = \sum_{rs} R_{(i+r)(j+s)} \kappa_{qrs} \quad (9)$$

where r and s are pixel indices corresponding to the column r and row s of the discrete kernel basis function κ_{qrs} defined by:

$$\kappa_{qrs} = \int_{s-\frac{1}{2}}^{s+\frac{1}{2}} \int_{r-\frac{1}{2}}^{r+\frac{1}{2}} \kappa_q(u, v) \, du \, dv \quad (10)$$

We refer to $[R \otimes \kappa_q]_{ij}$ as a *basis image* since it is the linear combination of these basis images modified by spatial polynomials and combined with the differential background that constitutes the target image model. A basis image $[R \otimes \kappa_q]_{ij}$ is calculated from the discrete convolution of the reference image R_{ij} with the corresponding discrete kernel basis function κ_{qrs} via Equation 9, which implies that the reference image R_{ij} must extend beyond the pixel domain of the target image I_{ij} . The discrete kernel basis function κ_{qrs} may be defined directly, or calculated by analytical or numerical integration of Equation 10 given a definition for $\kappa_q(u, v)$. Note that the terms for modelling the differential background in Equation 8 can be thought of as multiplying a basis image that is set to unity at all pixels.

All that is now required to fully define the model for the target image is to make a choice of suitable kernel basis functions, from which the corresponding basis images are derived. This is where

¹ Although not considered here, further orthogonalisation of the spatial polynomial terms could be achieved by using, for example, Gram-Schmidt orthogonalisation. However, the orthogonalisation can only ever be approximate as the dot products that define orthogonality use inverse-variance pixel weights, and the variances depend on the model being fitted (see Section 2.5).

different authors have made different choices (e.g. the Gaussian basis functions, the delta basis functions, etc.), and we leave the treatment of these choices to Section 3 where we consider their implications in more detail.

2.2 The Kernel Model

Assuming that we have a solution for the polynomial coefficients a_{qmn} of the kernel basis functions, we would like to know how to construct the discrete kernel model K_{rsij} at any pixel (i, j) in the target image. This is achieved by defining:

$$K_{rsij} = \int_{s-\frac{1}{2}}^{s+\frac{1}{2}} \int_{r-\frac{1}{2}}^{r+\frac{1}{2}} K(u, v, x_i, y_j) du dv \quad (11)$$

which, on substitution of Equations 2, 3 & 10, reduces to:

$$K_{rsij} = \sum_{q=1}^{N_K} \kappa_{qrs} \sum_{m=0}^{d_q} \sum_{n=0}^{d_q-m} a_{qmn} \eta_i^m \xi_j^n \quad (12)$$

2.3 Controlling The Spatial Variation Of The Photometric Scale Factor

The kernel sum $P_{ij} = \sum_{rs} K_{rsij}$, which in general is a function of spatial pixel (i, j) , defines the *photometric scale factor* between the reference image and the target image:

$$P_{ij} = \sum_{rs} \sum_{q=1}^{N_K} \kappa_{qrs} \sum_{m=0}^{d_q} \sum_{n=0}^{d_q-m} a_{qmn} \eta_i^m \xi_j^n \quad (13)$$

Our current formulation of the DIA problem in Section 2.1 is such that P_{ij} will vary across the image as a polynomial of degree equal to the maximum of the set of degrees $d_{\max} = \max_q \{d_q\}$ for the coefficients of the (sub-)set of kernel basis functions that have a non-zero sum. This can be seen by swapping the summation order in Equation 13 and combining the kernel basis function coefficients into a single set of coefficients a'_{mn} :

$$P_{ij} = \sum_{m=0}^{d_{\max}} \sum_{n=0}^{d_{\max}-m} a'_{mn} \eta_i^m \xi_j^n \quad (14)$$

where:

$$a'_{mn} = \sum_{q=1}^{N_K} a_{qmn} \sum_{rs} \kappa_{qrs} \quad (15)$$

This behaviour may be undesirable if we wish to employ a different degree of spatial variation in the photometric scale factor to the degree of spatial variation of the shape of the convolution kernel. A00 noted that those kernel basis functions with zero sums do not contribute to the spatial variation of the photometric scale factor, regardless of the spatial variation of their coefficients, and that one may always construct a new set of kernel basis functions that are a linear combination of the original set of basis functions.

We assume that our kernel basis functions have been normalised to a sum of unity, or have a zero sum, and that our first kernel basis function κ_{1rs} , without loss of generality, has a sum of unity. We then form a new set of kernel basis functions as follows:

$$\kappa'_{qrs} = \begin{cases} \kappa_{qrs} & \text{if } q = 1 \text{ or } \sum_{rs} \kappa_{qrs} = 0 \\ \kappa_{qrs} - \kappa_{1rs} & \text{if } q > 1 \text{ and } \sum_{rs} \kappa_{qrs} = 1 \end{cases} \quad (16)$$

It follows that all of our new kernel basis functions κ'_{qrs} have zero sums except for the first basis function κ'_{1rs} which has a sum of unity.

Adopting our new set of kernel basis functions and dropping the prime from our notation, the photometric scale factor P_{ij} reduces to:

$$P_{ij} = \sum_{m=0}^{d_1} \sum_{n=0}^{d_1-m} a_{1mn} \eta_i^m \xi_j^n \quad (17)$$

which is a polynomial in the spatial coordinates (x, y) of degree d_1 .

Hence, by transforming the kernel basis functions as outlined above, one may specify a polynomial degree d_1 of spatial variation for the photometric scale factor, associated only with the coefficient of the first kernel basis function, and which we redefine as the degree d_p . Collectively, the spatial variation of the kernel basis functions describes the kernel shape variations, and therefore the polynomial degree of spatial variation for the kernel shape is set by the value of $\max_q \{d_q\}$, which is always greater than or equal to d_p . This is an important point to understand since if one wants to model the situation where the kernel shape is expected to spatially vary with a smaller degree than the photometric scale factor, then one should still fit a model with $\min_q \{d_q\} = d_p$. For example, to model the situation where the kernel shape is spatially invariant between two images but the spatial transparency pattern varies linearly (e.g. because of changes in airmass gradient), then one must adopt a linear spatial variation for all of the kernel basis functions. This enables the spatial variations of the zero-sum kernel basis functions to offset the spatial variations in kernel shape induced by the spatial variations of the unit-sum kernel basis function.

To summarise, we have shown how to decouple the spatial variation of the photometric scale factor from the kernel shape variations (with the aforementioned caveat), which leads to three natural types of spatial variation in the DIA formulation; namely, photometric scale factor variations, differential background variations, and kernel shape variations, characterised by the degrees d_p , d_B , and $d_s = \max_q \{d_q\} \geq d_p$, respectively.

2.4 Fitting The Target Image Model

In order to fit the model in Equation 8 to the target image, we construct the chi-squared:

$$\chi^2 = \sum_{ij} \left(\frac{I_{ij} - M_{ij}}{\sigma_{ij}} \right)^2 \quad (18)$$

where the σ_{ij} represent the target image pixel uncertainties. Minimising the chi-squared in Equation 18 falls into the class of general linear least-squares problems, since the model in Equation 8 is linear with respect to the unknown coefficients a_{qmn} and b_{kl} to be determined. This class of problems has a standard solution procedure by construction of the *normal equations*. We refer the reader to the treatment of this subject in Numerical Recipes (Press et al. 2007) for more details.

The normal equations are most compactly represented by the matrix equation:

$$\mathbf{H}\boldsymbol{\alpha} = \boldsymbol{\beta} \quad (19)$$

where the square matrix \mathbf{H} is the least-squares matrix, the vector $\boldsymbol{\alpha}$ is the vector of model parameters, and $\boldsymbol{\beta}$ is another vector.

For each kernel basis function, there are $N_q = (d_q + 1)(d_q + 2)/2$ polynomial coefficients a_{qmn} , and for the differential background, there are $N_B = (d_B + 1)(d_B + 2)/2$ polynomial coefficients b_{kl} , leading to a total of $N_{\text{par}} = (\sum_q N_q) + N_B$ parameters to be determined. Hence the least-squares matrix \mathbf{H} is

of size N_{par} by N_{par} elements, and the vectors $\boldsymbol{\alpha}$ and $\boldsymbol{\beta}$ are of length N_{par} elements.

If we take z as a generalised index for all of the free parameters, then we are simply assigning a one-to-one correspondence $f: z \leftrightarrow (q, m, n, k, l)$ that specifies which coefficient, a_{qmn} or b_{kl} , corresponds to the current element α_z of the vector of parameters $\boldsymbol{\alpha}$. This mapping may order the parameters in an arbitrary way, but the ordering is only important for the efficient computation of \mathbf{H} and $\boldsymbol{\beta}$ if one does not pre-calculate all of the necessary polynomial and basis images (see Sections 5.1 & 5.2).

Following from the definition of the model for the target image in Equation 8, the elements of the least-squares matrix \mathbf{H} (i.e. the coefficients in the normal equations) and vector $\boldsymbol{\beta}$ may now be written out explicitly in terms of the basis images:

$$H_{zz'} = \begin{cases} \sum_{ij} \eta_i^{m+m'} \xi_j^{n+n'} [R \otimes \kappa_q]_{ij} [R \otimes \kappa_{q'}]_{ij} / \sigma_{ij}^2 & \text{for } \alpha_z \equiv a_{qmn} \text{ and } \alpha_{z'} \equiv a_{q'm'n'} \\ \sum_{ij} \eta_i^{m+k'} \xi_j^{n+l'} [R \otimes \kappa_q]_{ij} / \sigma_{ij}^2 & \text{for } \alpha_z \equiv a_{qmn} \text{ and } \alpha_{z'} \equiv b_{k'l'} \\ \sum_{ij} \eta_i^{k+m'} \xi_j^{l+n'} [R \otimes \kappa_{q'}]_{ij} / \sigma_{ij}^2 & \text{for } \alpha_z \equiv b_{kl} \text{ and } \alpha_{z'} \equiv a_{q'm'n'} \\ \sum_{ij} \eta_i^{k+k'} \xi_j^{l+l'} / \sigma_{ij}^2 & \text{for } \alpha_z \equiv b_{kl} \text{ and } \alpha_{z'} \equiv b_{k'l'} \end{cases} \quad (20)$$

$$\beta_z = \begin{cases} \sum_{ij} \eta_i^m \xi_j^n I_{ij} [R \otimes \kappa_q]_{ij} / \sigma_{ij}^2 & \text{for } \alpha_z \equiv a_{qmn} \\ \sum_{ij} \eta_i^k \xi_j^l I_{ij} / \sigma_{ij}^2 & \text{for } \alpha_z \equiv b_{kl} \end{cases} \quad (21)$$

Cholesky factorisation of the symmetric and positive-definite matrix \mathbf{H} , followed by forward and back substitution is the most efficient and numerically stable method (Golub & Van Loan 1996) for obtaining the solution $\boldsymbol{\alpha} = \hat{\boldsymbol{\alpha}}$ to the normal equations. Explicit calculation of the matrix inverse \mathbf{H}^{-1} is only strictly necessary if one requires the covariance matrix $\text{cov}(\hat{\alpha}_z, \hat{\alpha}_{z'}) = \{\mathbf{H}^{-1}\}_{zz'}$. We note that the calculation of the uncertainties in the elements of $\hat{\boldsymbol{\alpha}}$ is one such case since the uncertainty σ_z in each $\hat{\alpha}_z$ is given by:

$$\sigma_z = \sqrt{\{\mathbf{H}^{-1}\}_{zz}} \quad (22)$$

2.5 The Noise Model And Iteration

The calculation of the least-squares matrix \mathbf{H} and vector $\boldsymbol{\beta}$ requires the adoption of a suitable noise model for the target image pixel uncertainties σ_{ij} . B08 specify one such model as:

$$\sigma_{ij}^2 = \frac{\sigma_0^2}{F_{ij}^2} + \frac{M_{ij}}{GF_{ij}} \quad (23)$$

where σ_0 is the CCD readout noise (ADU), G is the CCD gain (e^-/ADU), and F_{ij} is the master flat-field image. This model assumes that both the master flat-field image F_{ij} and the reference image R_{ij} are noiseless, which is a reasonable assumption for such typically high signal-to-noise (S/N) images.

Most importantly, we note that in this noise model, the uncertainties σ_{ij} depend on the target image model M_{ij} and consequently, fitting M_{ij} as described in Section 2.4 becomes an iterative process². In the first iteration, it is appropriate to approximate

² Strictly speaking, the fact that the uncertainties σ_{ij} depend on the target image model M_{ij} also implies that minimising χ^2 is no longer equivalent to maximising the likelihood. The maximum likelihood estimator is obtained

M_{ij} by using I_{ij} , which enables the calculation of the initial kernel and differential background solution. In subsequent iterations, the current image model defined by Equation 8 should be used to set the σ_{ij} as per Equation 23. In Appendix B, we use an example to demonstrate the bias that can be introduced into the model parameters if the iterative fitting procedure is not performed (see also Section 4.1).

It is also desirable to employ a k -sigma-clip algorithm in order to prevent outlier target image pixel values from influencing the solution, including those from variable objects and cosmic ray events. This may easily be achieved by calculating the normalised residuals $\varepsilon_{ij} = (I_{ij} - M_{ij})/\sigma_{ij}$ and ignoring any pixels with $|\varepsilon_{ij}| \geq k$ in subsequent iterations. The reliability of the k -sigma-clip algorithm depends heavily on the accuracy of the adopted noise model, and since the initial σ_{ij} values are calculated using an approximation to M_{ij} , we recommend that the sigma-clipping commences at the second iteration.

Our final note in this Section is that the noise model in Equation 23 could be improved, specifically by considering the noise introduced by the reference image, which is non-negligible when the S/N of the reference image is similar to that of the target image. A00 and B08 have previously considered such a noise model. Here, we explicit a useful noise model for a target image and a combined reference image that have been registered to the nearest pixel (i.e. avoiding image resampling):

$$\sigma_{ij}^2 = \frac{\sigma_0^2}{F_{\text{tar},ij}^2} + \frac{M_{ij}}{GF_{\text{tar},ij}} + \sum_{rs} K_{rsij}^2 \sigma_{\text{ref},(i+r)(j+s)}^2 \quad (24)$$

with:

$$\sigma_{\text{ref},ij}^2 = \frac{1}{N_{\text{im}}^2} \sum_k \left[\frac{\sigma_0^2}{F_{\text{ref},kij}^2} + \frac{R'_{kij}}{GF_{\text{ref},kij}} \right] \quad (25)$$

where the R'_{kij} represent the N_{im} images that have been combined to create the reference image, and $F_{\text{tar},ij}$ and $F_{\text{ref},kij}$ are the master flat-field images corresponding to the target image and constituent images of the reference image, respectively.

2.6 The Input Data

Ideally, *every pixel* in the target image should be used in the calculation of \mathbf{H} and $\boldsymbol{\beta}$, and therefore contribute to the kernel and differential background solution. However, due to the nature of the convolution process, the target image model is undefined in a border of width equal to half the kernel width around the image edges if the reference image is the same size as the target image, and therefore these target image pixels cannot be used in the calculation of \mathbf{H} and $\boldsymbol{\beta}$. Also, “bad” pixels (e.g. bad columns/rows, hot pixels, saturated pixels, cosmic-ray events, etc.) should be excluded from the calculations, which means that any target image pixel (i, j) to be included in the calculation of \mathbf{H} and $\boldsymbol{\beta}$ should be “good” in the target image, and that all reference image pixels to be used for calculating the target image model at (i, j) should be “good” in the reference image. This implies that a bad pixel in the reference image can discount a set of pixels equal to the kernel area in the target image, and therefore, as suggested in B08, bad pixels in the reference image should be kept to a minimum, and kernels with excessively large footprints should be avoided when there are bad pixels in the reference image (e.g. see Section 2.3 of Bramich et al. 2011).

instead by minimising $\chi^2 + \sum_{ij} \ln(\sigma_{ij}^2)$, which renders the fitting of the target image model as a non-linear problem.

The areas of the target image which contain only sky background and no astronomical objects will only contribute information on the differential sky background coefficients in the target image model. Hence, one may limit the set of target image pixels to be used in the calculation of \mathbf{H} and $\boldsymbol{\beta}$ to a set of image sub-regions encompassing the higher S/N objects in the target image, which speeds the computations (fewer pixel values to be included in the required summations) while sacrificing some information. We note that contrary to the statements of some authors (e.g. M08), these sub-regions need not be centred on isolated stars. In fact, sub-regions of crowded high S/N objects (PSF-like or not) are precisely the image regions that contain the most information on the convolution kernel and differential background, because each pixel contains PSF and background information at a high S/N ratio.

2.7 Difference Images

We briefly mention that the definition of a difference image D_{ij} is:

$$D_{ij} = I_{ij} - M_{ij} \quad (26)$$

This image of residuals consists of noise (mainly Poisson noise from photon counting) and any differential flux from objects that have varied in brightness and/or position compared to the epoch of the reference image, since constant sources are fully subtracted during the DIA process. However, if an inappropriate kernel and/or differential background model is chosen, then unwanted systematic errors will leave signatures in the difference image as large-amplitude high-spatial-frequency residuals at the positions of the brighter objects (for inappropriate kernel models), and as lower-amplitude low-spatial-frequency deviations in the difference image background from zero (for inappropriate differential background models). We note that if a reliable noise model exists, then the normalised difference image ε_{ij} defined by:

$$\varepsilon_{ij} = \frac{I_{ij} - M_{ij}}{\sigma_{ij}} \quad (27)$$

acts as a useful guide to the level of flux variation in any one pixel, since the pixel values in this image are in units of sigma-deviations.

The purpose of producing a difference image is to enable accurate differential photometry to be performed in the absence of PSF crowding for all objects of interest (constant and variable). The object positions are presumed known from analysis of the reference image or from fitting of the differential flux on the difference image.

3 COMMON BASIS FUNCTION CHOICES

In this Section, we elucidate the common choices for the kernel basis functions. We stress that since the choice of basis functions is fully independent of the DIA framework presented in the previous Section, the generation of a set of basis functions may be implemented as code that is completely separate from the DIA code.

3.1 The Gaussian Basis Functions

A98 introduced the *Gaussian basis functions* as a set of two-dimensional radially-symmetric Gaussian functions of different widths, each one modified by a polynomial of the kernel coordinates of a certain degree. The justifications for this choice are that an instrumental PSF is approximated by a Gaussian to first order, the convolution of a Gaussian by a Gaussian is also a Gaussian, and

that a Gaussian decays rapidly beyond a given distance. The user is required to specify the number of Gaussian functions N_{gau} , and then for each Gaussian function (indexed by λ), the user must specify the width $\sigma_{\text{gau},\lambda}$ and the degree of the modifying polynomial $D_{\text{gau},\lambda}$. It follows that the definition of the q th kernel basis function corresponding to the λ th Gaussian with a modifying polynomial term of degree $d_{\text{gau},u}$ and degree $d_{\text{gau},v}$ in the u and v coordinates, respectively, is given by:

$$\kappa_q(u, v) = u^{d_{\text{gau},u}} v^{d_{\text{gau},v}} e^{-(u^2+v^2)/2\sigma_{\text{gau},\lambda}^2} \quad (28)$$

where $0 \leq d_{\text{gau},u} + d_{\text{gau},v} \leq D_{\text{gau},\lambda}$. The number of kernel basis functions N_{K} in this prescription is given by:

$$N_{\text{K}} = \sum_{\lambda=1}^{N_{\text{gau}}} \frac{(D_{\text{gau},\lambda} + 1)(D_{\text{gau},\lambda} + 2)}{2} \quad (29)$$

The Gaussian basis functions need to be numerically integrated via Equation 10 to form the corresponding discrete kernel basis functions, and then subsequently they should be transformed as detailed in Section 2.3 to allow control over the spatial variation of the photometric scale factor. Finally, we note that the adoption of a set of Gaussian kernel basis functions does not provide any simplification in the calculation of the basis images $[R \otimes \kappa_q]_{ij}$ via Equation 9.

Typical specifications for the Gaussian basis functions in the literature usually include three Gaussian functions, and the ISIS2.2³ software developed by A98 and A00 adopts Gaussian widths of 0.7, 2.0, and 4.0 pix with modifying polynomials of degrees 6, 4, and 3, respectively, by default, resulting in 53 Gaussian basis functions. Israel, Hessman & Schuh (2007) investigated how the optimal choice of Gaussian basis functions depends on the properties of the images for which DIA is to be performed (e.g. seeing, S/N, etc.), and although they manage to give some general recommendations, there seems to be no unique answer. It has also been noted by Yuan & Akerlof (2008) that the radial symmetry of the Gaussian functions may not be appropriate for elliptical PSFs, although it would be trivial to expand the Gaussian basis function definition in Equation 28 to include elliptical two-dimensional Gaussians with an arbitrary centre and axis orientation.

3.2 The Delta Basis Functions

Let us introduce the definition of the Kronecker delta-function δ_{ij} :

$$\delta_{ij} = \begin{cases} 1 & \text{if } i = j \\ 0 & \text{if } i \neq j \end{cases} \quad (30)$$

Let us also assume that there exists a one-to-one correspondence $g : q \leftrightarrow (\mu, \nu)$ which associates the q th kernel basis function with the discrete kernel pixel coordinates (μ, ν) such that, without loss of generality, $q = 1 \Leftrightarrow (\mu, \nu) = (0, 0)$. Then we may directly define the q th discrete kernel basis function κ_{qrs} by:

$$\kappa_{qrs} = \begin{cases} \delta_{r0} \delta_{s0} & \text{for } q = 1 \\ \delta_{r\mu} \delta_{s\nu} - \delta_{r0} \delta_{s0} & \text{for } q > 1 \end{cases} \quad (31)$$

where we have already included the transformation as detailed in Section 2.3 to allow control over the spatial variation of the photometric scale factor. It is clear that when $q = 1$, κ_{1rs} obtains the value of 1 at $(r, s) = (0, 0)$ and 0 elsewhere, and that when $q > 1$,

³ <http://www2.iap.fr/users/alard/package.html>

κ_{qrs} obtains the value of 1 at $(r,s) = (\mu, \nu)$, -1 at $(r,s) = (0,0)$, and 0 elsewhere. Thus κ_{1rs} adds flux to the PSF core, and the other κ_{qrs} subtract flux from the core and add it back at displaced locations.

We refer to this set of kernel basis functions as the *delta basis functions*. The set of delta basis functions may be chosen to cover any discrete kernel domain (e.g. circular - B08, square - M08, etc.) by defining the number of kernel basis functions N_κ and the mapping g appropriately.

The basis images corresponding to the delta basis functions have a conveniently simple form that may be derived by substituting Equation 31 into Equation 9 and including a product of delta-functions to combine the two cases into one expression:

$$[R \otimes \kappa_q]_{ij} = R_{(i+\mu)(j+\nu)} + (\delta_{\mu 0} \delta_{\nu 0} - 1) R_{ij} \quad (32)$$

Hence, the first basis image is the reference image itself, and the remaining basis images are each formed by shifting the reference image by the appropriate integer-pixel shift, and then subtracting the non-shifted reference image. This has important speed and memory implications when implementing the calculation of the least-squares matrix and vector (see Section 5).

B08 introduced the idea of solving directly for the kernel pixel values K_{rs} of a spatially invariant kernel. We note that if we take $\kappa_{qrs} = \delta_{r\mu} \delta_{s\nu}$ for all q as an alternative definition for the discrete kernel basis functions in Equation 31, then the corresponding basis images are given by $[R \otimes \kappa_q]_{ij} = R_{(i+\mu)(j+\nu)}$. This definition ignores any control that we may wish to exercise over the photometric scale factor, but this is not an issue when considering a spatially invariant kernel (as in B08). Substitution of this new result for the basis images into Equations 20 & 21, and assuming that the kernel and differential background are spatially invariant, leads directly to the least-squares matrix and vector derived by B08 from their direct solution approach. Hence, adoption of the delta basis functions in the A98 DIA framework is equivalent to solving directly for the kernel pixel values. A similar line of argument extends this conclusion to spatially variable kernels.

The delta basis functions require minimal information from the user about the kernel shape and size for their specification. However, the dependence of the optimal kernel shape and size on the reference and target image properties has not yet been investigated, although it is clear that the greater the difference in PSF width between the images, the larger the size of the convolution kernel that is required to match the PSFs.

3.3 The Mixed-Resolution Delta Basis Functions

The number of delta basis functions, and hence the number of coefficients a_{qmn} , grows as the number of kernel pixels, which in turn grows as the square of the kernel radius. Since the least-squares matrix is a square matrix of size N_{par} by N_{par} elements, the number of elements to be calculated in the least-squares matrix grows as the kernel radius to the fourth power. Hence, the time taken to calculate the solution for the coefficients a_{qmn} and b_{kl} increases considerably when solving for larger kernels.

To address this performance issue, Albrow et al. (2009) introduced the idea of ‘‘binned’’ kernel pixels in the outer part of the kernel on the assumption that the kernel shows slower variations of smaller amplitude beyond a certain radius. Specifically, they introduced 3×3 binned kernel pixels beyond a kernel radius of 7 pix to replace the single kernel pixels, which greatly reduces the number of parameters to be solved for while maintaining a sufficiently large kernel. For example, for a circular kernel of radius 13 pix, which fits in a square array of 27 by 27 pixels, there are 577 single kernel

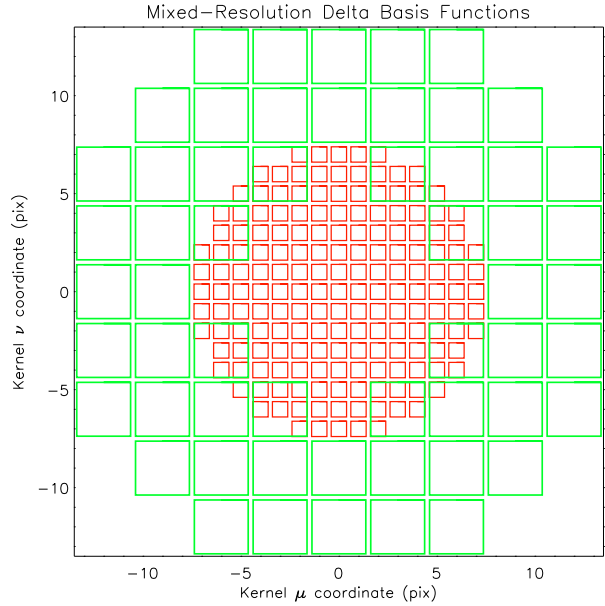


Figure 1. The distribution of single (red) and 3×3 binned (green) kernel pixels for a circular kernel of radius 13 pix that uses 3×3 binned kernel pixels beyond a radius of 7 pix.

pixels. Adopting the 3×3 binned kernel pixels beyond a radius of 7 pix results in 233 parameters, of which 177 are single kernel pixels and 56 are 3×3 binned kernel pixels. The number of elements to be calculated in the least-squares matrix is consequently reduced to $\sim 16\%$ without compromising the extent of the kernel model. Figure 1 shows the distribution of single (red) and 3×3 binned (green) kernel pixels for this example.

We generalise the idea of a binned kernel pixel to that of an *extended delta basis function* defined by:

$$\kappa_{qrs} = \begin{cases} (1/N_{\text{pix},q}) + (\delta_{\mu 0} \delta_{\nu 0} - 1) \delta_{r0} \delta_{s0} & \text{for } (r,s) \in S_q \\ (\delta_{\mu 0} \delta_{\nu 0} - 1) \delta_{r0} \delta_{s0} & \text{for } (r,s) \notin S_q \end{cases} \quad (33)$$

where S_q is the set of kernel pixels spanned by the extended delta basis function (of any shape and spatial distribution), and $N_{\text{pix},q}$ is the number of elements in S_q . Note that we have assumed that the one-to-one correspondence $g : q \leftrightarrow (\mu, \nu)$ is defined with $q = 1 \leftrightarrow (\mu, \nu) = (0, 0)$. Again, we have forced the sum of the extended delta basis function to be unity if it is the first kernel basis function ($q = 1$), and to be zero if it is not ($q > 1$), in order to be able to exercise control over the spatial variation of the photometric scale factor.

The basis image corresponding to the extended delta basis function defined in Equation 33 is easily derived by substitution into Equation 9:

$$[R \otimes \kappa_q]_{ij} = \frac{1}{N_{\text{pix},q}} \left[\sum_{(r,s) \in S_q} R_{(i+r)(j+s)} \right] + (\delta_{\mu 0} \delta_{\nu 0} - 1) R_{ij} \quad (34)$$

Therefore, this basis image is formed by averaging $N_{\text{pix},q}$ versions of the reference image with each one shifted by the appropriate integer-pixel shift, and then subtracting the non-shifted reference image (except if this is the first basis image). Again, this has important speed and memory implications when implementing the calculation of the least-squares matrix and vector (see Section 5). We note that the basis images corresponding to the 3×3 binned ker-

nel pixels from Albrow et al. (2009) are formed from integer-pixel shifted versions of a box-car smoothed reference image.

We refer to a set of basis functions as *mixed-resolution* if they include any combination of delta basis functions and extended delta basis functions, and we emphasise that extended delta basis functions need not be square and they may be of any shape (e.g. circles, rectangles, rings, arcs, etc.). We also note that the delta basis function is a special case of the extended delta basis function, and that overlapping extended delta basis functions are acceptable in a set of kernel basis functions as long as none of the extended delta basis functions may be constructed as a linear combination of any of the other kernel basis functions. If this condition is not met, then the solution for the coefficients in the target image model is degenerate. Finally, we mention that mixed-resolution delta basis functions have the potential to be used in kernels with an adaptive resolution, which is a subject that has not yet been investigated in terms of its application to DIA.

4 VALIDATING AND DEMONSTRATING THE ALGORITHM

So far we have only examined the theory of our general DIA formulation. We now proceed to validate the algorithm using simulated images. We also demonstrate the ability of the algorithm to correct for a spatially varying differential transparency across the image area using real data.

4.1 Simulated Image Data

Our first task is to check that the algorithm can recover the exact model coefficients used to generate a set of simulated image data without any artificial noise added to the pixel values. By doing this we are validating our DIA formulation by confirming that there are no degeneracies in the target image model that we did not foresee.

We generate a reference image of size 1000×1000 pix with a constant sky level of 1000 ADU and with 5000 stars. The stars are generated using a Gaussian PSF with a full-width half-maximum (FWHM) of 4 pix, pixel coordinates drawn from a uniform distribution over the detector area, and log-fluxes drawn from a uniform distribution between 2 and 5 (i.e. stars have fluxes between 10^2 and 10^5 ADU). The image parameters that we have chosen are actually not important, and the tests in the absence of artificial noise give the same results so long as there are at least a few stars spread out over the image.

We then generate a set of target images from the reference image using Equation 8 for various sets of kernel basis functions (Gaussian, delta, and mixed-resolution) and values for the corresponding coefficients, and for all combinations of d_p , d_B , and d_S (defined in Section 2.3) taken from the set $\{0, 1, 2, 3\}$. We find that when we fit each target image with the model used to generate it, we can recover the exact input values (to within numerical precision) of the coefficients a_{qm} and b_{kl} in Equation 8 for all cases. Hence we confirm that our algorithm works and that there are no hidden degeneracies.

Next we generate a set of target images from the reference image by convolving the reference image with a spatially varying kernel of polynomial degree d'_S with the kernel normalised to a unit sum at each pixel. Then we multiply the convolved reference image with a polynomial surface of degree d'_p representing the photometric scale factor and we add a polynomial surface of degree d'_B representing the differential background. We have done this for all

combinations of d'_p , d'_B , and d'_S taken from the set $\{0, 1, 2\}$. In this set up, the degree of spatial variation of the kernel shape is actually $d'_p + d'_S$ since the polynomial surface for the photometric scale factor multiplies the kernel pixel values which also spatially vary as a polynomial. Therefore, the appropriate (linear) target image model has $d_p = d'_p$, $d_B = d'_B$, and $d_S = d'_p + d'_S$, and when we adopt such a model we find that we can recover the exact values for the model coefficients (again to within numerical precision). If we naively set $d_p = d'_p$, $d_B = d'_B$, and $d_S = d'_S$ for our target image model, then the algorithm does not manage to perfectly fit the target image, leaving significant residuals.

Now we consider how the algorithm performs for simulated images with added artificial noise. We adopt the same reference image as before and we use delta basis functions with $d_1 = d_p = 1$ and $d_q = d_S = 2$ for all $q > 1$. We define the kernel model to be a square array of 7×7 pixels. The target image model coefficients are arbitrarily chosen and specifically we set $a_{1mn} = \{1.1, 0.3, 0.1\}$ for $(m, n) = \{(0, 0), (1, 0), (0, 1)\}$. Also, we define $d_B = 0$ and set $b_{00} = 100$. We then use all of these definitions in Equation 8 to generate a noiseless target image S_{ij} .

From the noiseless target image S_{ij} , we generate 10^3 noisy versions. Each noisy target image I_{ij} is formed by generating a 1000×1000 pixel image Σ_{ij} of values drawn from a normal distribution with zero mean and unit σ , and then computing:

$$I_{ij} = S_{ij} + \Sigma_{ij} \sqrt{\sigma_0^2 + S_{ij}} \quad (35)$$

where the coefficient of Σ_{ij} is derived from Equation 23 for $G = 1 e^-/\text{ADU}$ and $F_{ij} = 1$. We adopt a reasonable value for the read-out noise of $\sigma_0 = 5$ ADU. For each noisy target image, we fit the same model used to generate the noiseless target image, employing the iterative scheme described in Section 2.5 (but without sigma-clipping).

In the plots along the diagonal of Figure 2, we show the distributions of the coefficients a_{1mn} for $(m, n) = \{(0, 0), (1, 0), (0, 1)\}$ and b_{00} as derived from the fits to the 10^3 noisy target images. The red and black histograms represent the coefficient distributions after the first and third iterations, respectively, and the reason for iterating the solution is clear; namely, approximating M_{ij} with I_{ij} in the noise model in Equation 23 in the first iteration introduces a significant bias into the fitted coefficients (in this example b_{00} is underestimated by ~ 1 ADU or $\sim 1\%$; see also Appendix B). We also report in the plots the measured mean and standard deviation of each coefficient distribution after the third iteration. The measured means of the coefficient distributions are an excellent match to the input coefficient values (no differences to at least 5 significant figures), and the measured standard deviations are an excellent match to the formal uncertainties in the coefficients reported by the algorithm (calculated via Equation 22 and displayed as ‘‘Sigma’’). For the coefficient distributions after the third iteration, we fit a Gaussian with mean and sigma equal to the corresponding input coefficient value and the formal uncertainty in the coefficient, respectively, and we plot the Gaussian fits as the blue curves. One can see that the coefficient distributions follow the Gaussian distributions very well.

In the off-diagonal plots of Figure 2, we show scatter plots for all of the coefficient pairs that can be formed from a_{100} , a_{110} , a_{101} , and b_{00} using the results of the fits to the 10^3 noisy target images. The red and black points represent the fitted coefficients after the first and third iterations, respectively. In each plot we also display the formal 1σ -error ellipses (blue curves) as provided by the covariance matrix of the fit (see Section 2.4). It is encouraging to see that there are virtually no correlations between the target image model

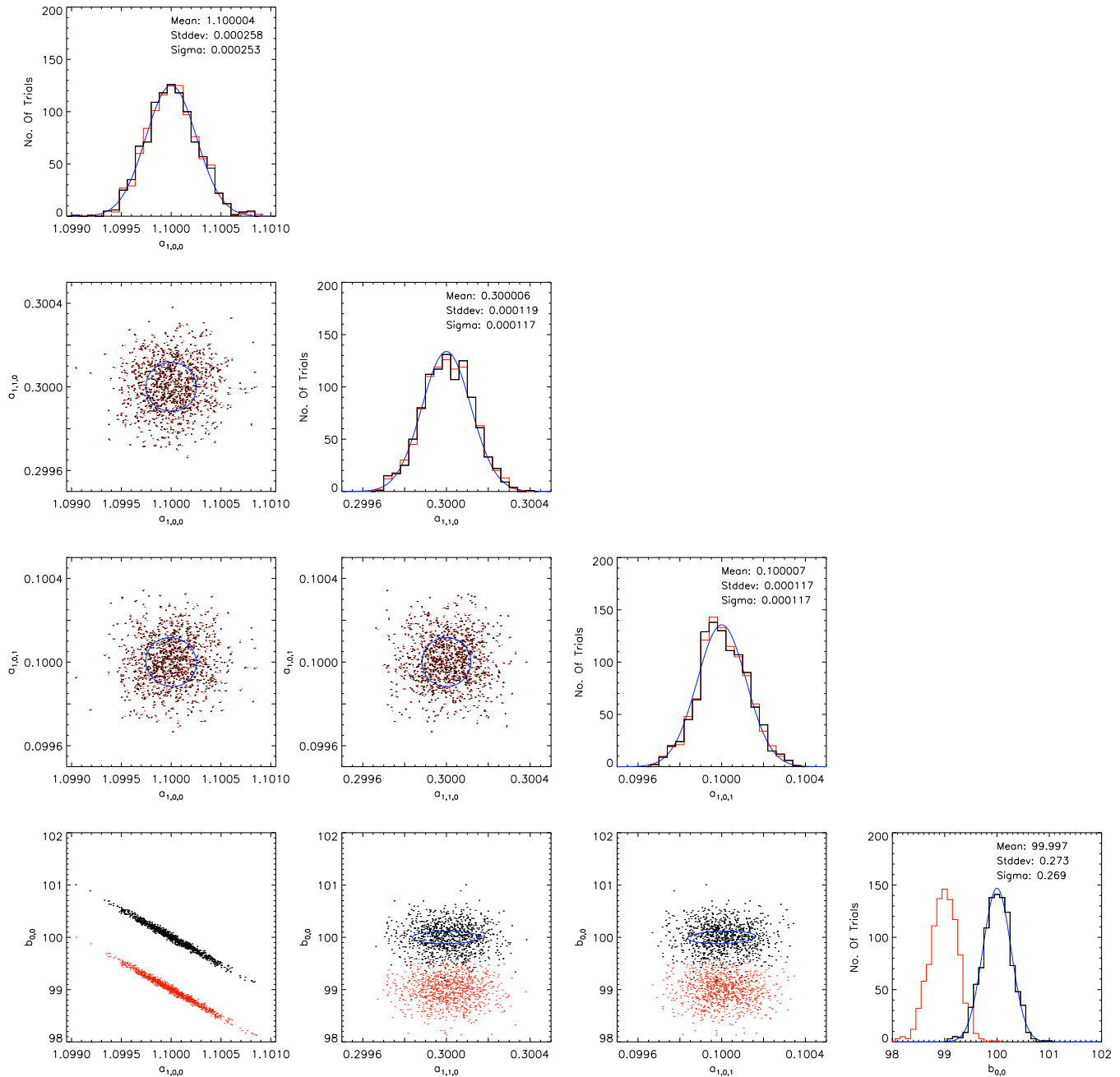


Figure 2. Plots along the diagonal: Histograms of the coefficients a_{1mn} for $(m,n) = \{(0,0), (1,0), (0,1)\}$ and b_{00} as derived from the fits to the 10^3 noisy target images. The red and black histograms represent the coefficient distributions after the first and third iterations, respectively. The blue curves are fitted Gaussian distributions centred on the input coefficient values and with widths equal to the formal uncertainties in the coefficients. **Off-diagonal plots:** Scatter plots for all of the coefficient pairs that can be formed from a_{100} , a_{110} , a_{101} , and b_{00} using the results of the fits to the 10^3 noisy target images. The red and black points represent the fitted coefficients after the first and third iterations, respectively. The blue curves are formal 1σ -error ellipses.

coefficients a_{100} , a_{110} , and a_{101} associated with the spatial variation of the photometric scale factor, or between the differential background coefficient b_{00} and a_{110} or a_{101} . Also, as expected, there is a strong anti-correlation between the zeroth-order coefficients for the photometric scale factor and the differential background, a_{100} and b_{00} .

The anti-correlation between a_{100} and b_{00} is a well-known feature of DIA that occurs when the reference image includes a non-zero background level. The kernel basis functions with non-

zero sums in the target image model (Equation 8) serve to blur *and scale* the reference image, including the background level, and hence the model terms for the differential background must compensate for this effect in the opposite sense. The consequence is that if the photometric scale is overestimated, then the differential background will be underestimated to compensate, and vice versa. To minimise the amplitude of this anti-correlation, we recommend subtracting the sky background from the reference image before applying DIA (as suggested by B08 in their Section 2.2), a procedure

which could also include the subtraction of the spatially varying components of the background (i.e. to flatten the background).

The results of our investigations in this Section lead us to conclude that our DIA algorithm is working exactly as expected for simulated images with added artificial noise.

4.2 Real Image Data

We demonstrate our DIA algorithm using a pair of calibrated images from a commercial telescope (Celestron 8-inch Schmidt-Cassegrain $f = 2032$ mm) and CCD camera (Kodak KAF-1603ME) with a pixel scale of ~ 1.8 arcsec/pix, a FOV of 0.26×0.26 degrees, and no filter. We designate one of the images as the reference image and the other as the target image. Since both images are undersampled, it is necessary to pre-blur them before applying DIA. We blur the reference and target images with Gaussian convolution kernels of FWHMs 3.5 and 4.0 pix, respectively.

The target image was chosen specifically because it was taken through light clouds. We cropped the images appropriately in order to register them to the nearest pixel. We display the reference and target images in the top two panels of Figure 3 with the same linear scale and dynamic range of 700 ADU. The black regions are masked pixels that cover saturated stars. To the right of each image, we show three magnified image stamps corresponding to the red boxes marked in each image. These image stamps contain some of the brightest stars in the images which are most suitable for inspecting the quality of the difference images in the following tests.

We proceed to fit the target image using the reference image and a set of delta basis functions representing a square kernel array of size 9×9 pixels. After some experimentation with different values for d_p , d_B , and d_S , we find that the differential background is only satisfactorily modelled for $d_B \geq 3$. The resulting difference images for each combination of d_p and d_S taken from the set $\{0, 1\}$ and with $d_B = 3$ are displayed in the middle four panels of Figure 3, all with the same linear scale. The complicated residuals in the differential sky background are apparent in all cases.

For $(d_p, d_B, d_S) = (0, 3, 0)$, the dominant residuals at the star positions show an under-subtraction of the star fluxes towards the top-right of the difference image, and an over-subtraction of the star fluxes towards the bottom-left, which is clearly due to the presence of spatial transparency variations that are not modelled by the spatially invariant photometric scale factor. This is also the case for $(d_p, d_B, d_S) = (0, 3, 1)$, but since the kernel model is allowed to vary in shape across the image area, the zero-sum delta basis functions try to mitigate the spatial transparency variations by moving flux from the reference image background to the star PSF for those stars whose fluxes are under-subtracted, and by moving flux from the star PSF to the reference image background for those stars whose fluxes are over-subtracted, resulting in smaller residuals at the star positions but with the residuals spread out over a larger area. This is most visible in the image stamps on the right which still show under- and over-subtraction of the star fluxes, but spread out over more pixels. Setting $(d_p, d_B, d_S) = (1, 3, 0)$ successfully removes the under- and over-subtraction of the star fluxes from the difference images, but instead leaves positive-negative residuals at each star position whose orientation is a function of position, which is a consequence of not modelling spatial variations in the kernel shape.

Adopting $(d_p, d_B, d_S) = (1, 3, 1)$ produces difference images where only the brightest stars can be seen to be mildly under- or over-subtracted, which is a much better result than what current DIA algorithms are capable of producing (i.e. the $(d_p, d_B, d_S) = (0, 3, 1)$ case). It is quite possible that further improvements in

the difference image residuals may be obtained by adopting even higher polynomial degrees for d_p , d_B , and d_S , but a full optimisation of the production of the difference image in our example is outside of the scope of this paper.

In the bottom two panels of Figure 3, we reproduce the fitted photometric scale factor and differential background as a function of position over the image area which show that the atmospheric transparency diminishes and the sky background brightens for the parts of the target image that are more affected by clouds. This result is to be expected since clouds attenuate the incoming light from outside the Earth's atmosphere, but they also increase the local sky brightness by scattering ambient light (e.g. light pollution, moon light, etc.) back to the ground.

However, to be absolutely sure that this observed anti-correlation is not an artefact of our modelling procedure, we performed the following test. We cut out ten well-distributed image stamps around bright stars from the reference image, and we also cut out the corresponding stamps from the target image. For each pair of image stamps, we proceeded to fit the target image stamp using the reference image stamp and the same kernel configuration that we used to model the full target image, and we adopted a spatially invariant kernel and differential background (i.e. $(d_p, d_B, d_S) = (0, 0, 0)$). We compared the photometric scale factor and the differential background derived from each fit, which represent robust local estimates of these quantities, to the predicted values of these quantities at the stamp coordinates from our model for the full target image, and we found a very good agreement (to within ~ 2 -4 per cent). This confirms that the results from our new DIA algorithm are fully consistent with the results that can be obtained using current DIA algorithms.

This real data example has served as a proof-of-concept where we have demonstrated that we can use our DIA algorithm to successfully model a spatially varying photometric scale factor. We have also shown how the results of solving for a spatially invariant kernel and differential background for small image sub-regions (stamps) in different parts of the image can be used to perform consistency checks on the solution for the target image model from our DIA algorithm.

5 IMPLEMENTATION HINTS AND OPTIMISATION TRICKS

Producing difference images is a very computationally intensive task, especially when modelling a spatially varying kernel as we have described in Section 2. However, many applications of DIA require quick (within seconds or minutes) processing of the target images (e.g. robotic searches for anomalies in microlensing events towards the Galactic bulge - RoboNet-II - Tsapras et al. 2009, supernovae searches - Palomar Transient Factory - Gal-Yam et al. 2011, etc.). Hence the optimisation of the calculations required to produce the difference images is an important aspect of DIA. In the following subsections, we describe some useful optimisation tricks that may be used to obtain some substantial improvements in speed, and that have the potential to rival brute force DIA implementations on graphical processing units (GPUs; Fluke et al. 2011).

5.1 Memory Considerations

Firstly we consider what information needs to be stored in computer memory to enable the efficient calculation of the least-squares matrix \mathbf{H} and vector $\boldsymbol{\beta}$, and the target image model M_{ij} . We limit

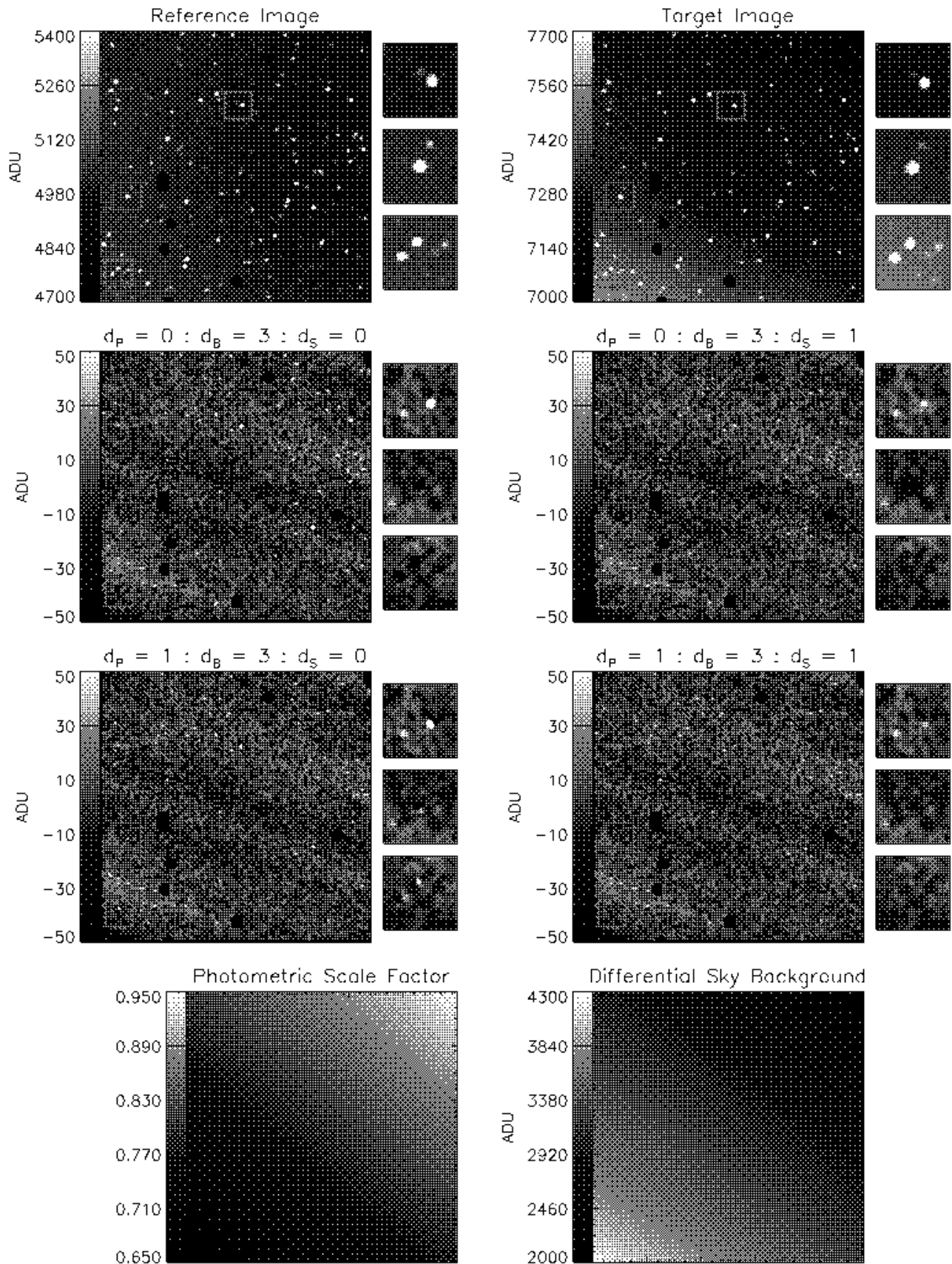


Figure 3. Top: A pair of calibrated images where the target image (right) was taken through light clouds. Middle: Difference images for various target image models. The red boxes are displayed as magnified image stamps to the right of each difference image. Note that in the bottom-left hand corner of the upper image stamp, the positive-negative residuals are caused by a moving object. Bottom: The spatial dependence of the fitted photometric scale factor and differential background for the target image model with $(d_P, d_B, d_S) = (1, 3, 1)$. See text for more details.

ourselves to considering arrays that are of the size of the target image, since the other information that needs to be stored in computer memory (e.g. the discrete kernel basis functions κ_{qrs}) takes up negligible space in comparison.

For efficiency, we need to pre-calculate and store in computer memory those images that will be used more than once in the calculation of the difference image. In the general case, these images are the target image I_{ij} , the reference image R_{ij} , the inverse-variance image $1/\sigma_{ij}^2$, the N_κ basis images $[R \otimes \kappa_q]_{ij}$, and the N_{poly} polynomial images of the spatial coordinates $\eta_i^m \xi_j^n$ for $m+n \geq 1$. If d_{max} is the maximum degree of the polynomial spatial variation of the kernel basis function coefficients and the differential background, then the maximum degree of the polynomial images of the spatial coordinates in the least-squares matrix \mathbf{H} is $2d_{\text{max}}$ (see Equation 20), which implies that:

$$N_{\text{poly}} = [(2d_{\text{max}} + 1)(2d_{\text{max}} + 2)/2] - 1 = d_{\text{max}}(2d_{\text{max}} + 3) \quad (36)$$

For the Gaussian basis functions, with the typical choice of 53 such functions (see Section 3.1), it is perfectly feasible to store all of the corresponding basis images in computer memory (e.g. 53 floating point 2000×2000 pixel images take up ~ 831 Mb of memory using IDL). Furthermore, the spatial variation of the kernel basis function coefficients is not usually modelled with a higher degree polynomial than a cubic polynomial, and a cubic polynomial variation requires $N_{\text{poly}} = 27$. Again, it is possible to store all of the required $1 + 1 + 1 + 53 + 27 = 83$ images in computer memory (e.g. 83 floating point 2000×2000 pixel images take up ~ 1280 Mb of memory using IDL).

For the delta basis functions, a typical circular kernel of radius 10 pix generates 349 basis images, which is a more problematic number of images to store in the computer memory (especially for a 32-bit machine). However, the basis images for the delta basis functions may be generated without performing a computationally-costly convolution by simply subtracting the reference image from a shifted version of itself (see Equation 32). Hence, if one is prepared to recalculate each basis image as needed, and assuming that up to 27 polynomial images are required, then only $1 + 1 + 1 + 1 + 27 = 31$ images need to be stored in computer memory. Similarly, using the same approach for mixed-resolution delta basis functions with N_{res} resolutions only requires the storage of N_{res} versions of the reference image, each one produced by convolving the original reference image with a box-car of the shape of the relevant extended delta basis function.

5.2 Calculating The Least-Squares Matrix

By far, most of the arithmetic operations required to fit the target image model and produce a difference image are performed in the construction of the least-squares matrix \mathbf{H} and vector $\boldsymbol{\beta}$. In fact, assuming that the inverse-variance, basis, and polynomial images are pre-calculated, and that D is the polynomial degree of spatial variation of each kernel basis function and the differential background, then there are $N_{\text{par}} = (N_\kappa + 1)(D + 1)(D + 2)/2$ coefficients to be determined, and brute force computation of \mathbf{H} requires the calculation of N_{par}^2 entries, where the vast majority of these entries require $3N_{\text{pix}}$ multiplications and $N_{\text{pix}} - 1$ additions (note that N_{pix} is the number of target image pixels that are being modelled). Furthermore, $\boldsymbol{\beta}$ requires the computation of another N_{par} entries, where again the vast majority of these entries require $3N_{\text{pix}}$ multiplications and $N_{\text{pix}} - 1$ additions. Hence, the number of arithmetic operations N_{op} for the brute force computation of \mathbf{H} and $\boldsymbol{\beta}$, normalised by N_{pix} ,

is given by:

$$N_{\text{op}} \approx 4N_{\text{par}}(N_{\text{par}} + 1) \quad (37)$$

We have already mentioned in Section 2.6 that limiting the target image pixels to be used in calculating \mathbf{H} and $\boldsymbol{\beta}$ to a set of suitable image sub-regions minimises the number of required arithmetic operations for minimal loss of precision on the coefficients in the target image model. This clearly follows from the discussion in the previous paragraph.

We have also noted in Section 2.4 that \mathbf{H} is symmetric. This means that in reality only $N_{\text{par}}(N_{\text{par}} + 1)/2$ entries in \mathbf{H} need to be calculated, and that the number of arithmetic operations reduces to:

$$N_{\text{op}} \approx 2N_{\text{par}}(N_{\text{par}} + 3) \quad (38)$$

Now we consider the order in which we may efficiently calculate the entries of \mathbf{H} and $\boldsymbol{\beta}$, and since \mathbf{H} has the much larger number of entries, our choice is driven by the structure of \mathbf{H} . Note that in the following, we treat the differential background as having a corresponding basis image set to unity at all pixels (see Section 2.1). Inspection of Equation 20 for \mathbf{H} reveals that one has the choice of either:

- (i) For each of the $(N_{\text{poly}} + 1)$ polynomial images, cycle through the $(N_\kappa + 1)^2$ pairs of basis images to calculate the corresponding $(N_\kappa + 1)^2$ and $N_\kappa + 1$ entries in \mathbf{H} and $\boldsymbol{\beta}$, respectively.
- (ii) For each of the $(N_\kappa + 1)^2$ pairs of basis images, cycle through the $(N_{\text{poly}} + 1)$ polynomial images to calculate the corresponding $[(D + 1)(D + 2)/2]^2$ and $(D + 1)(D + 2)/2$ entries in \mathbf{H} and $\boldsymbol{\beta}$, respectively.

We note that to calculate each entry in \mathbf{H} , a pair of basis images needs to be multiplied together before performing the required summation, whereas the polynomial images are already pre-calculated from the coordinate images in computer memory, and therefore option (ii) is the most efficient because it minimises the number of the image multiplications that are required. Furthermore, in the case of the delta basis functions, the basis images are calculated as needed, and therefore option (ii) also minimises the number of times that each basis image must be calculated.

Having justified the choice of option (ii) for the order in which we should calculate the entries of \mathbf{H} and $\boldsymbol{\beta}$, we adopt a corresponding parameter ordering in the parameter vector $\boldsymbol{\alpha}$ that leads to the structure for \mathbf{H} that we illustrate in Figure 4 for $N_\kappa = 15$ (artificially small for clarity) and $D = 2$. The matrix \mathbf{H} is made up of $(N_\kappa + 1)^2$ square sub-matrices (top panel of Figure 4), where each sub-matrix corresponds to the product of a single basis image pair $[R \otimes \kappa_q]_{ij} [R \otimes \kappa_q']_{ij}$. Furthermore, each square sub-matrix has $[(D + 1)(D + 2)/2]^2$ entries, where each entry corresponds to a different polynomial image. However, within a single sub-matrix, there are only $N_{\text{poly}} + 1 = (D + 1)(2D + 1)$ independent entries (Equation 36; bottom panel of Figure 4). In our specific example for $D = 2$, there are 15 independent entries out of 36 entries in each sub-matrix (i.e. less than half of the entries need to be calculated).

The discovery of this property of \mathbf{H} is exceptionally important because it greatly decreases the number of required calculations. Neither M08 nor Quinn, Clocchiatti & Hamuy (2010) mention this optimisation, and A00 claim that the full modelling of the spatial variation of the kernel “quickly becomes intractable”, and that “order 3 requires roughly 100 times more calculations than a constant kernel solution”. We find that capitalising on the pattern in the sub-matrices of \mathbf{H} for a spatial variation of the kernel of degree 3, one would only require $N_{\text{poly}} + 1 = 28$ times more calculations than for

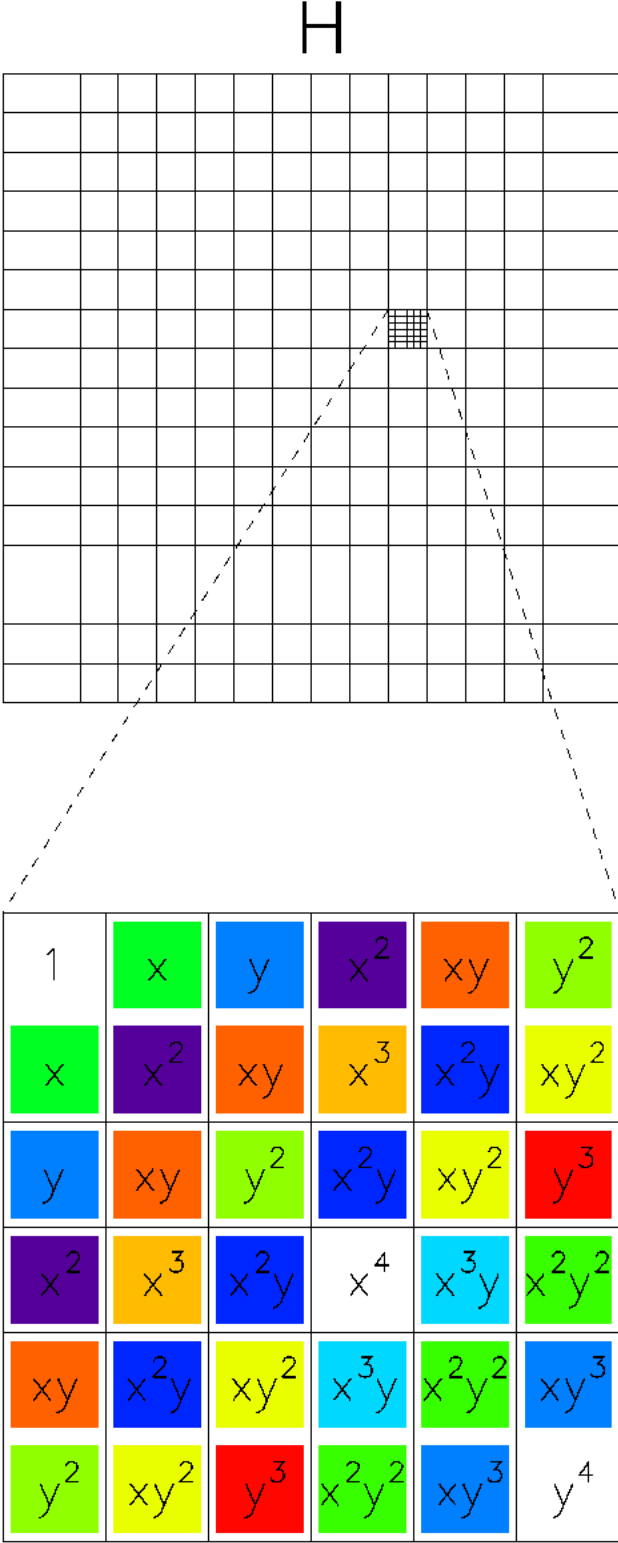


Figure 4. Top: The full least-squares matrix \mathbf{H} divided up into $(N_{\kappa} + 1)^2$ square sub-matrices, where each sub-matrix has $[(D+1)(D+2)/2]^2$ entries. For this example we have adopted an artificially small value of $N_{\kappa} = 15$ for clarity, and $D = 2$. Bottom: A magnified view of a single square sub-matrix. Each sub-matrix in \mathbf{H} has the same structure. Entries in the sub-matrix that employ the same polynomial image in their calculation have the same background colour (except for the single entries corresponding to the polynomial images 1 , η_i^4 , and ξ_j^4). The polynomial term marked in each sub-matrix entry indicates the degree in the spatial coordinates (x, y) of the polynomial image corresponding to that entry.

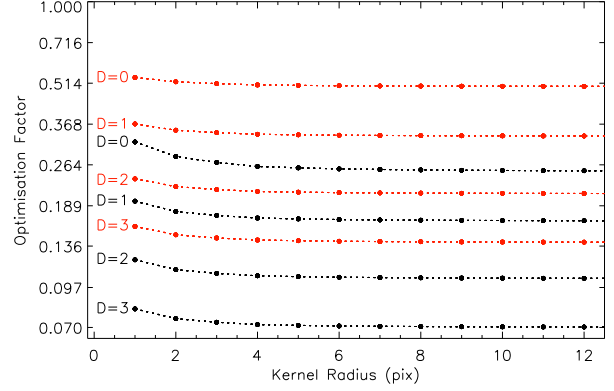


Figure 5. Plot of the ratio of the number of arithmetic operations required to calculate \mathbf{H} and $\boldsymbol{\beta}$ for our optimised algorithm compared to the same quantity for the brute force computation (black), and for the brute force computation that capitalises on the symmetry in \mathbf{H} (red), when we adopt a set of delta basis functions representing a circular kernel. These ratios are plotted as a function of the kernel radius (pix) and for $D = 0, 1, 2$, and 3 .

a constant kernel solution, which is a very significant improvement in the potential performance of the algorithm.

We are now in a position to develop an optimised algorithm for computing \mathbf{H} and $\boldsymbol{\beta}$. We propose the following procedure:

- (i) For each row of square sub-matrices in \mathbf{H} , carry out steps (ii)–(vii), and then finish.
- (ii) Calculate $[R \otimes \kappa_q]_{ij} / \sigma_{ij}^2$ and $I_{ij} [R \otimes \kappa_q]_{ij} / \sigma_{ij}^2$ for the current row, which requires $2N_{\text{pix}}$ multiplications.
- (iii) For each sub-matrix in the current row that lies on the diagonal or in the upper half of \mathbf{H} , carry out steps (iv)–(v), and then move on to step (vi).
- (iv) Calculate $[R \otimes \kappa_q]_{ij} [R \otimes \kappa_{q'}]_{ij} / \sigma_{ij}^2$ for the current sub-matrix, which requires N_{pix} multiplications.
- (v) For each pre-calculated polynomial image, calculate the expression $\sum_{ij} \eta_i^{m+m'} \xi_j^{n+n'} [R \otimes \kappa_q]_{ij} [R \otimes \kappa_{q'}]_{ij} / \sigma_{ij}^2$, which requires N_{pix} multiplications (except for $m+m'+n+n'=0$) and $N_{\text{pix}} - 1$ additions, and fill out the relevant entries of the current sub-matrix.
- (vi) Fill out the entries of the sub-matrices in the current row that lie in the lower half of \mathbf{H} by using the fact that \mathbf{H} is symmetric, which takes a negligible number of operations.
- (vii) For each relevant pre-calculated polynomial image, calculate the expression $\sum_{ij} \eta_i^m \xi_j^n I_{ij} [R \otimes \kappa_q]_{ij} / \sigma_{ij}^2$, which requires N_{pix} multiplications (except for $m+n=0$) and $N_{\text{pix}} - 1$ additions, and fill out the corresponding entries in $\boldsymbol{\beta}$.

We now attempt to estimate the number of arithmetic operations that are required to calculate \mathbf{H} and $\boldsymbol{\beta}$ using our optimised algorithm. Observe that step (ii) is repeated $N_{\kappa} + 1$ times, steps (iv) and (v) are each repeated $(N_{\kappa} + 1)(N_{\kappa} + 2)/2$ times of which step (v) requires $\sim (2N_{\text{pix}})N_{\text{poly}} + N_{\text{pix}}$ arithmetic operations, and step (vii) is repeated $N_{\kappa} + 1$ times and requires $\sim (2N_{\text{pix}})[(D+1)(D+2)/2] - N_{\text{pix}}$ arithmetic operations. Using $N_{\text{poly}} = D(2D+3)$, then we derive the number of arithmetic operations in our optimised algorithm, normalised by N_{pix} , to be:

$$N_{\text{op}} \approx (N_{\kappa} + 1) \left[N_{\kappa}(D+1)(2D+1) + 5D^2 + 9D + 5 \right] \quad (39)$$

In Figure 5, for $D = 0, 1, 2$, and 3 , we plot in black the ratio of the expression in Equation 39 to the expression in Equation 37 as a function of the kernel radius (pix) for a set of delta basis functions

representing a circular kernel. We see that for typical kernel radii of ~ 8 -12 pix, we expect that our optimised algorithm will reach an efficiency in the number of arithmetic operations of ~ 0.251 , 0.167 , 0.104 , and 0.070 compared to the brute force computation for $D=0, 1, 2$, and 3 , respectively. Also, in Figure 5, for $D=0, 1, 2$, and 3 , we plot in red the ratio of the expression in Equation 39 to the expression in Equation 38 as a function of the kernel radius (pix) for the same set of delta basis functions. We further conclude that our optimised algorithm will reach an efficiency in the number of arithmetic operations of ~ 0.501 , 0.334 , 0.209 , and 0.140 compared to the brute force computation that capitalises on the symmetry in \mathbf{H} for $D=0, 1, 2$, and 3 , respectively.

6 CONCLUSIONS

The general framework presented in this paper treats the problem of matching the PSF, photometric scaling, and sky background between two images, where each of these components varies as a polynomial of the spatial coordinates. Where this paper improves over previous works on DIA are as follows:

- We demonstrate how to model a spatially varying photometric scale factor within our framework, which is a new concept that will be important for DIA applied to wide-field imaging data that may suffer transparency and airmass variations across the field-of-view.
- We show how to decouple the spatial variation of each kernel basis function, the photometric scale factor, and the differential background from each other, which allows more control over the level of spatial variation of each component in the target image model.
- In Section 2 we develop what we hope is a clear notation and logical order for the DIA equations and methodology aimed at aiding others in creating DIA software implementations.
- We prove the equivalence of adopting delta basis functions for the kernel model and solving directly for the kernel pixel values (B08).
- We introduce the mixed-resolution delta basis functions with the aim of reducing the size of the least-squares problem to be solved when using delta basis functions, and we elucidate their properties and implications for DIA.
- We present some important optimisations in the calculation of the least-squares matrix which lead to a reduction in the number of arithmetic operations that need to be performed for typical kernel radii of ~ 8 -12 pix to $\sim 16.7\%$, $\sim 10.4\%$, and $\sim 7.0\%$ compared to the brute force computation for linear, quadratic, and cubic spatial variations, respectively, of the target image model.

ACKNOWLEDGEMENTS

Dedicated to my three stars $\star\star\star$.

The research leading to these results has received funding from the European Union Seventh Framework Programme (FP7/2007-2013) under grant agreement numbers 229517 and 268421. We thank the Qatar Foundation for support via QNRF grant NPRP-09-476-1-78.

APPENDIX A

Here we show that the convolution of the reference image R_{ij} with a continuous kernel basis function $\kappa_q(u, v)$ may be calculated as a discrete convolution.

Firstly, consider the definition of continuous convolution applied to the convolution of the reference image:

$$[R \otimes \kappa_q](x, y) = \int_{-\infty}^{\infty} \int_{-\infty}^{\infty} R(x+u, y+v) \kappa_q(u, v) du dv \quad (40)$$

where $R(x, y)$ is a continuous representation of the reference image.

Over the area of one pixel with coordinates (x_i, y_j) , the value of the reference image is a constant, i.e. $R(x, y) = R_{ij}$ for $x_i - 1/2 \leq x < x_i + 1/2$ and $y_j - 1/2 \leq y < y_j + 1/2$, and therefore:

$$[R \otimes \kappa_q](x_i, y_j) = \sum_{rs} R_{(i+r)(j+s)} \int_{s-\frac{1}{2}}^{s+\frac{1}{2}} \int_{r-\frac{1}{2}}^{r+\frac{1}{2}} \kappa_q(u, v) du dv \quad (41)$$

where r and s are integer indices varying over the domain where the kernel basis function achieves non-zero values.

Adopting the notation $[R \otimes \kappa_q]_{ij}$ for the image $[R \otimes \kappa_q](x_i, y_j)$, then we may write:

$$[R \otimes \kappa_q]_{ij} = \sum_{rs} R_{(i+r)(j+s)} \kappa_{qrs} \quad (42)$$

$$\kappa_{qrs} = \int_{s-\frac{1}{2}}^{s+\frac{1}{2}} \int_{r-\frac{1}{2}}^{r+\frac{1}{2}} \kappa_q(u, v) du dv \quad (43)$$

where r and s now represent the pixel indices corresponding to the column r and row s of the discrete kernel basis function κ_{qrs} .

Hence, the image $[R \otimes \kappa_q](x, y) = [R \otimes \kappa_q]_{ij}$, which we refer to as a *basis image*, may be calculated via the discrete convolution defined in Equation 42.

APPENDIX B

We wish to briefly investigate the consequences of approximating M_{ij} with I_{ij} in the noise model in Equation 23 as opposed to iterating the solution and using the current image model from Equation 8 to update the noise model at each iteration. For this purpose we use the software developed in B08 for the case of a kernel and differential background that are both spatially invariant.

We create a 205×205 pixel noiseless reference image R_{ij} by setting a constant sky level of 1000 ADU and adding in 100 objects, each of flux 10^5 ADU and with a two-dimensional Gaussian profile of FWHM 4 pix, at random spatial coordinates drawn from a uniform distribution across the image area. We also create a 201×201 pixel noiseless target image S_{ij} by convolving the R_{ij} with a discrete 5×5 pixel kernel calculated via numerical integration of Equation 10 for a two-dimensional Gaussian of FWHM 2 pix centred at the kernel centre and normalised to a sum of unity.

We then perform the following experiment, adopting reasonable values for the readout noise and gain of $\sigma_0 = 5$ ADU and $G = 1 e^-/\text{ADU}$, respectively:

- (i) We generate a 201×201 pixel image Σ_{ij} of values drawn from a normal distribution with zero mean and unit σ , and we construct a noisy target image I_{ij} via:

$$I_{ij} = S_{ij} + \Sigma_{ij} \sqrt{\sigma_0^2 + S_{ij}} \quad (44)$$

where the coefficient of Σ_{ij} is derived from Equation 23 for $G = 1 e^-/\text{ADU}$ and $F_{ij} = 1$.

(ii) We solve for a kernel and differential background that are both spatially invariant to match the reference image R_{ij} to the target image I_{ij} . For the kernel model, we adopt 25 delta basis functions covering a 5×5 pixel array to match the actual domain of the discrete pixel kernel used to generate S_{ij} from R_{ij} . For the target image noise model σ_{ij} we use Equation 23 with M_{ij} approximated by I_{ij} .

(iii) We record the photometric scale factor P_1 and differential background B_1 of the solution obtained in step (ii).

(iv) We iterate the solution for the spatially invariant kernel and differential background three times (sufficient for convergence), each time using the current image model M_{ij} calculated via Equation 8 to set the target image noise model σ_{ij} via Equation 23.

(v) Again we record the photometric scale factor P_2 and differential background B_2 of the solution obtained during the final iteration in step (iv).

We repeat the above experiment 10^5 times and calculate the mean and standard deviation of each of the quantities P_1 , B_1 , P_2 , and B_2 . We find that $\langle P_1 \rangle - 1 = 5.38 \times 10^{-6} \pm 1.68 \times 10^{-6}$ and $\langle B_1 \rangle = -1.0085 \pm 0.0020$ ADU, where the uncertainty in the mean is estimated from the standard deviation divided by $\sqrt{10^5}$. The correct solution in our experiment should have a photometric scale factor of unity and a differential background of zero. Clearly, solving the DIA problem using the data to estimate the uncertainties on the pixel values in the target image introduces a bias of ~ 1 ADU in the differential background (and a very slight bias in the photometric scale factor). Hence one cannot assume that the background in the difference images produced using this method is zero, and aperture photometry on such difference images should include the computation and subtraction of a local background, and PSF photometry should include the local background as a parameter in the fit. The bias in the differential background solution, which corresponds to an underestimated sky background in the target image model, is easily explained by the fact that the background pixels in the target image that randomly have smaller values than the true sky background are given more weight (or smaller uncertainties) in the fit than those background pixels that randomly have larger values than the true sky background.

For the case where we iteratively solve the DIA problem using the current image model to determine the uncertainties on the target image pixel values at each iteration, we find that $\langle P_2 \rangle - 1 = 1.98 \times 10^{-6} \pm 1.68 \times 10^{-6}$ and $\langle B_2 \rangle = -0.0031 \pm 0.0020$ ADU. Therefore, at the precision of our experiment (which is well beyond the photometric precision typically obtained for real data), we conclude that there is no bias in the derived photometric scale factor or differential background for this method, which validates the iterative method presented in Section 2.5.

Finally we mention that even though we only report one particular experiment in this Appendix, we actually performed a range of experiments on artificial noisy target images generated with different set-ups (e.g. different convolution kernels) and we found similar results in all cases.

REFERENCES

- Alard C. & Lupton R.H., 1998, ApJ, 503, 325
 Alard C., 2000, A&AS, 144, 363
 Albrow M.D. et al., 2009, MNRAS, 397, 2099
 Bramich D.M., 2008, MNRAS, 386, L77

- Bramich D.M., Figuera Jaimes R., Giridhar S. & Arellano Ferro A., 2011, MNRAS, 413, 1275
 Fluke C.J., Barnes D.G., Barsdell B.R. & Hassan A.H., 2011, PASA, 28, 15
 Gal-Yam A. et al., 2011, ApJ, 736, 159
 Golub G.H. & Van Loan C.F., 1996, Matrix Computations, Third Edition, p140-147, p238-239
 Israel H., Hessman F.V. & Schuh S., 2007, AN, 328, 16
 Kaiser N. et al., 2010, Proc. SPIE, 7733, 12
 Law N.M. et al., 2009, PASP, 121, 1395
 Miller J.P., Pennypacker C.R. & White G.L., 2008, PASP, 120, 449
 Press W.H., Teukolsky S.A., Vetterling W.T. & Flannery B.P., 2007, Numerical Recipes: The Art Of Scientific Computing, Third Edition, p788-791
 Quinn J.L., Clocchiatti A. & Hamuy M., 2010, MNRAS, 403, 1
 Rau A. et al., 2009, PASP, 121, 1334
 Tsapras Y. et al., 2009, AN, 330, 4
 Yuan F. & Akerlof C.W., 2008, ApJ, 677, 808